Nanoscale

PAPER

View Article Online
View Journal | View Issue

Cite this: *Nanoscale*, 2019, **11**, 16968

Titanium silicalite as a radical-redox mediator for high-energy-density lithium–sulfur batteries†

Dan Chan,‡[a] Zhubing Xiao,‡[b] Zeqing Guo,[a] Yuchong Lai,[a] Yonggui Zhang,[a] Suya Zhou,[a] Xingwei Ding,[a] Huagui Nie[a] and Zhi Yang *[a]

Received 5th August 2019,
Accepted 2nd September 2019

DOI: 10.1039/c9nr06700k

rsc.li/nanoscale

Lithium–sulfur (Li–S) batteries are receiving intense interest owing to their high energy densities, cost effectiveness, and the natural abundance of sulfur. However, practical applications are still limited by rapid capacity decay caused by multielectron redox reactions and complex phase transformations. Here, we include commercially available titanium silicalite-1 (TS-1) in carbon/sulfur cathodes, to introduce strong chemical interactions between the lithium polysulfides (LiPS) and TS-1 in a working Li–S battery. *In situ* UV-visible spectroscopy together with other experimental results confirm that incorporation of TS-1 mediators enables direct conversion between S_8^{2-} and $S_3^{\bullet-}$ radicals during the discharge process, which effectively promotes the kinetic behaviors of soluble LiPS and regulates uniform nucleation and growth of solid sulfide precipitates. These features give our TS-1 engineered sulfur cathode an ultrahigh initial capacity of 1459 mA h g^{-1} at 0.1C. Moreover, the system has an impressively high areal capacity (3.84 mA h cm^{-2}) and long cycling stability with a high sulfur loading of 4.9 mg cm^{-2}. This novel and low-cost fabrication procedure is readily scalable and provides a promising avenue for potential industrial applications.

Introduction

To meet ever-growing demands for portable electronics and electric vehicles, lithium–sulfur (Li–S) batteries have been recognized as promising substitutes for conventional lithium-ion batteries, owing to their high theoretical capacity (1675 mA h g^{-1}) and energy density (2600 W h kg^{-1}), together with the high abundance and low-toxicity of sulfur.[1–4] However, the large-scale production and commercial applications of Li–S batteries have been hindered by some critical issues. Notably, the ready dissolution of lithium polysulfide (LiPS) intermediates leads to rapid capacity degradation.[5] Moreover, arbitrary diffusion of LiPS redistributes solid discharge products on electrode/electrolyte interfaces, passivating active surfaces and introducing a large overpotential for sulfur redox conversion.[6] Additionally, the intrinsic low electronic conductivity of sulfur and the solid discharge products (Li_2S or Li_2S_2) also result in sluggish redox kinetics and a low sulfur utilization.[7]

In the past decade, considerable efforts have been made to develop carbonaceous sulfur hosts (including porous carbon, doped graphene), and some conductive inorganic materials (including transition metal sulfides, carbides and nitrides) to tackle these problems.[8–16] These approaches have improved the rate capacity and cycling stability of Li–S batteries to a great extent. However, despite these achievements, most publications have focused on electrodes with impractically low sulfur loadings, less than 4 mg cm^{-2}, which is the threshold areal capacity requirement for electrical vehicles based on modern lithium ion batteries.[17] Although recently explored "self-supporting" cathodes have achieved higher sulfur loading and areal capacity, deviation from industry-standard slurry-coating techniques could require prohibitive reworking of traditional battery manufacturing processes and face problems with practicality.[18,19] Moreover, the low yield, laborious overall synthetic procedures, and high costs of anchoring materials such as nitrides, phosphides, MXene phases, Pt, and Au are economic and environmental drawbacks, which limit practical large-scale applications.[8] In this context, there remains an urgent need for novel anchoring materials to engineer the interfaces in the conversion process of LiPS and develop simpler and more cost-effective methods to boost the electrochemical performance of sulfur cathodes and push Li–S chemistry closer to commercial viability.

Titanium silicalite-1 (TS-1), an important member of the family of crystalline microporous materials, has attracted considerable attention owing to its low cost, high stability, and

[a]*Key Laboratory of Carbon Materials of Zhejiang Province, College of Chemistry and Materials Engineering, Wenzhou University, Wenzhou, 325035, PR China. E-mail: yang201079@126.com*
[b]*Henan Key Laboratory of Photovoltaic Materials, Henan University, Kaifeng, 475004, China*

†Electronic supplementary information (ESI) available. See DOI: 10.1039/c9nr06700k

‡These authors contributed equally to this work.

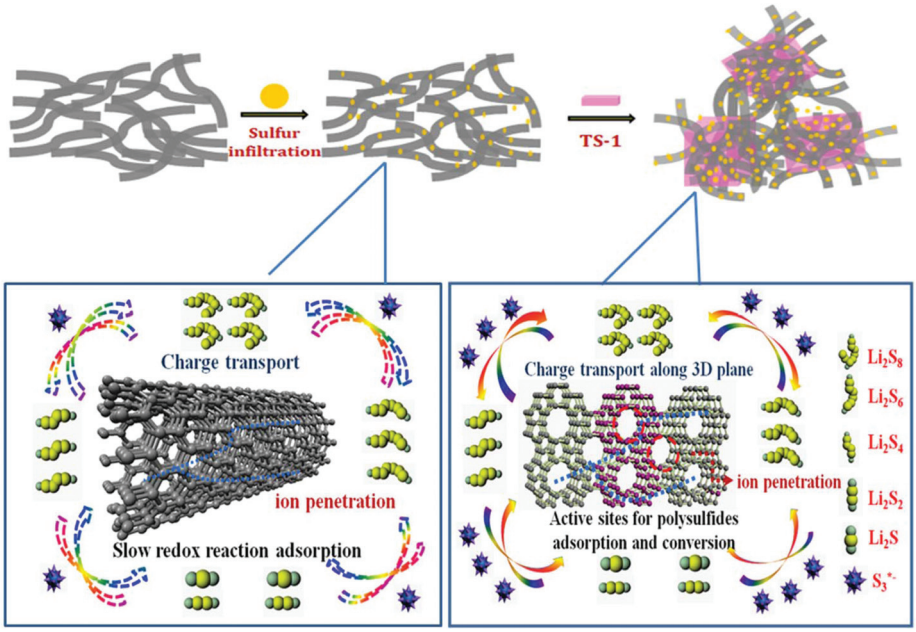

Fig. 1 Schematic illustration of the synthetic procedure for CNTs-S/TS-1 electrode.

excellent redox catalytic properties in numerous friendly environmental applications. In particular, TS-1 has been used in the oxidation of many organic compounds (including thiophene), and widely investigated for use as an oxidative desulfurization catalyst in recent years. The active Ti species of tetrahedrally coordinate titanium has excellent binding with the sulfur in thiophene leading to high catalytic performance.[20–22] On this basis, we considered that TS-1 might also efficiently convert LiPS in the cathode of Li–S batteries. Herein, we aimed to address the main issues facing Li–S batteries and the limitations of current composite cathodes mentioned above. We demonstrate for the first time, a novel strategy to develop highly stable sulfur electrodes with the use of commercially available TS-1 with redox catalytic properties. Such a TS-1 is capable of markedly enhancing the redox reactivity of LiPS owing to strong chemisorption, and highly active electrocatalysis that can regulate the kinetic behaviors of LiPS intermediates and growth of solid Li_2S in a working Li–S battery (Fig. 1). Furthermore, we used *in situ* UV-vis spectra to confirm that TS-1 alters the redox reactions of sulfur species through a $S_3^{\bullet-}$ radical-mediated process, which is highly favorable for improving sulfur utilization.[23] We attributed these features to the electrode, which exhibits an ultrahigh initial capacity of 1459 mA h g^{-1} at 0.1C. Importantly, the electrode with a higher sulfur loading of 4.9 mg cm^{-2} delivers a reversible areal capacity of 2.68 mA h cm^{-2} (546 mA h g^{-1}) over 200 cycles.

Results and discussion

The TS-1 containing hybrid cathode was simply constructed by depositing commercially available TS-1 as a carbon nanotube-sulfur (CNT-S) composite during the slurry-coating process, as schematically illustrated in Fig. 1. The resultant cathode is denoted CNT-S/TS-1 hereafter. The crystal structure and morphological characterization of TS-1 are presented in Fig. S1–S3 (ESI†). The lateral size of TS-1 was approximately 400 nm with a specific surface area as high as 355 m^2 g^{-1} (Fig. S2 and S3†). The strong polarity and high specific surface provide ample active sites for the coupled physical and chemical entrapment of LiPS. An optimized mass fraction of 17% for the TS-1 was used in the hybrid cathode (see details in the Experiment section), as indicated by Fig. S4.† Li–S cells were then fabricated and examined to enable validation of the detailed material properties and the sophisticated host–guest interactions. For comparison, we also investigated a CNT-S electrode with an identical sulfur content (63%) (Fig. S5†).

Typical cyclic voltammetry (CV) profiles for the CNT-S/TS-1 electrodes were first measured within a potential window 1.5–3.0 V (Fig. 2a). In the cathodic scan, two characteristic reduction peaks at 2.30 and 2.02 V were assigned to the reduction of elemental sulfur to high-order LiPS (Li_2S_x, $3 \leq x \leq 8$) and solid sulfides, respectively. In the reverse scanning, a strong peak at 2.38 V and a shoulder at 2.42 V are associated with coupled conversion of solid sulfides to LiPS intermediates and then to sulfur, respectively.[24] The slight variation for both the reduction and oxidation peaks in the second cycle might result from rearrangement of active sulfur from its original position to more energetically stable sites.[25] After the second cycle, the CV curves exhibited good overlap of the redox peaks, indicative of exceptional reversibility. Notably, the reduction peaks with the CNT-S/TS-1 cathode appeared at a higher potential than that of the CNT-S cathode (Fig. 2b and Fig. S6†). This distinguishable positive shift in the reduction peaks and the

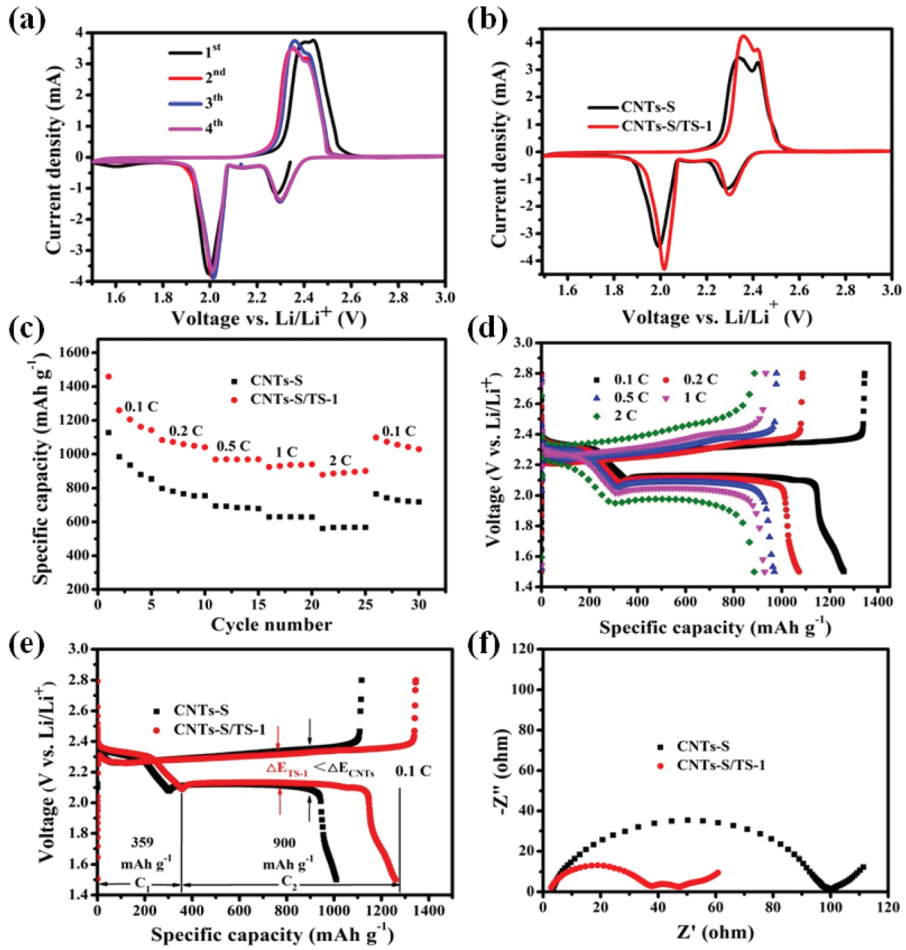

Fig. 2 Electrochemical performance of Li–S batteries. (a) CV curves of CNTs-S/TS-1 electrode. (b) CV curves of CNTs-S, and CNTs-S/TS-1 electrodes. (c) Rate performance at different current densities of CNTs-S, and CNTs-S/TS-1 electrodes. (d) Galvanostatic charge–discharge profiles of CNTs-S/TS-1 cathode at various current rates. (e) The first charge–discharge profiles of the CNTs-S, CNTs-S/TS-1 electrodes at 0.1C. (f) EIS plots of CNTs-S/TS-1 and CNTs-S electrodes.

negative shift in the oxidation peaks of the CNT-S/TS-1 cathode suggest that incorporation of TS-1 has a favorable influence on the Li–S electrochemistry. In addition, the collection coefficient (defined as the ratio of the peak area associated with the formation of solid sulfides at lower potentials to that associated with formation of LiPS at higher potentials) of CNT-S/TS-1 cathode was calculated to be 2.82, which is greater than that of 2.66 for the CNT-S cathodes (Table S1†).[26] These observations suggest that TS-1 has good catalytic activity and that it improves the redox reaction kinetics of LiPS.

Fig. 2c compares the rate performances of CNT-S/TS-1 and CNT-S electrodes under various current rates from 0.1 to 2C. Remarkably, the CNT-S/TS-1 electrode delivered an ultrahigh discharge capacity of 1459 mA h g^{-1}, which is approximately 87.1% of the theoretical capacity of a Li–S battery, indicating efficient utilization of sulfur. At current densities of 0.2, 0.5, 1, and 2C, high reversible capacities of 1062 1083, 968, 923, and 877 mA h g^{-1} were achieved, respectively. Importantly, as the current density was decreased to 0.1C, the large capacity of 1097 mA h g^{-1} indicated a highly reversible rate performance. In sharp contrast, the CNT-S electrode exhibited an inferior discharge capacity and poorer stability under the same conditions. In Fig. 2d, the discharge profile exhibited two discharge plateaus at 2.35 and 2.1 V, and the charge profiles showed one broad charge plateau between 2.2 and 2.45 V. These results were consistent with those from CV measurements (Fig. 2a). As the current rate was increased to 2C, the charge/discharge profiles retained the typical features of elemental sulfur and the potential polarization (ΔE) increased only slightly. Additionally, compared with the CNT-S electrode, the CNT-S/TS-1 showed a flatter plateau with a higher capacity and a lower potential polarization (Fig. 2e), further indicating the kinetically efficient reaction propelled by TS-1. The EIS measurements after different cycle states were further recorded and the detailed parameters and equivalent circuit fittings are illustrated in Fig. S7.† Fig. S7b and d† show Nyquist plots for the CNT-S/TS-1 and CNT-S electrodes after different cycles. According to the fitting results in Fig. S7e,† unlike the single semicircle observed in the high-frequency region for the CNT-S electrode, the Nyquist curves of the CNT-S/TS-1 electrode had

one semicircle in the medium frequency range, which corresponded to interfacial conversion reactions between TS-1 and LiPS. Interestingly, the R_{p2}//CPE values for the CNT-S/TS-1 electrode diminished gradually from 0 to 150 cycles. This decrease of the impedance might be attributed to optimization of the reaction interface in the chemical activation process.[27,28] Furthermore, the CNT-S/TS-1 electrode had a lower R_{p1}//CPE value, implying close contact and better coverage between the active material and the host.[29] This result was confirmed by examining the cycled devices. As depicted in Fig. S8,† an uniform precipitation and even coverage of active materials with no agglomerates are observed on the surface of TS-1 for the cycled CNT-S/TS-1 electrode. In sharp contrast, only sparse sulfur signal and obvious aggregation are detected in the cycled CNT-S electrode. These observations indicate that the TS-1 induces a controlled and uniform growth of Li_2S species on the surface of the composite instead of random deposition.

The cycling performances of the samples were further investigated at a current density of 1C, as shown in Fig. 3a. The CNT-S/TS-1 electrode exhibited a high initial discharge capacity of 905 mA h g^{-1}, which was maintained at 679 mA h g^{-1} after 240 cycles, corresponding to an average capacity decay rate as low as 0.062% per cycle, which was much lower than that of the CNT-S electrode. These results suggest that the incorporation of polar TS-1 into the interlaced CNT conductive network enabled effective physical confinement and chemical absorption on LiPS, contributing to utilization of sulfur and retardation of the shuttle effect. Furthermore, the TS-1 also regulated the long-term cycling stability of Li–S batteries. As shown in Fig. 3b, the CNT-S/TS-1 cathode at 0.5C delivered an initial discharge capacity of 798 mA h g^{-1} and a capacity of approximately 400 mA h g^{-1} was achieved at the 980th cycle. Long-term cycling stability ~1000 cycles at a low current rate of 0.5C for a CNT-based sulfur cathode has rarely been reported.

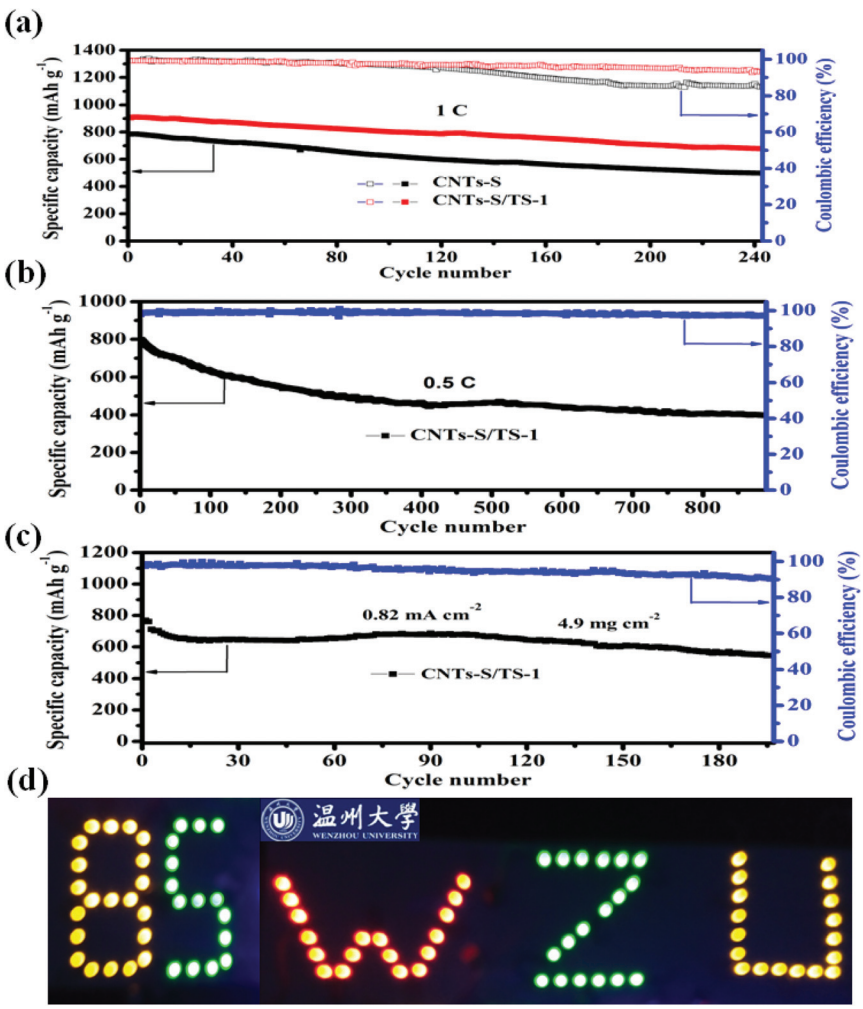

Fig. 3 Electrochemical performance of Li–S batteries. (a) Cycling stability of CNTs-S and CNTs-S/TS-1 electrode at 1C. (b) Long-term cycling performance of CNTs-S/TS-1 electrode at electrode 0.5C. (c) Cycling performance of CNTs-S/TS-1 electrode at current density of 0.82 mA cm^{-2} with area sulfur loading of 4.9 mg cm^{-2}. (d) The digital photograph of five CNTs-S/TS-1 batteries in series can light up 90 of 2835 LED modules (nominal voltage of 12 V and nominal power of 3 W).

A high sulfur loading is necessary for high-energy density Li–S batteries to meet commercial requirements. The above mentioned features suggest that incorporation of TS-1 may also exert positive impacts on the high-loaded sulfur electrode. Herein, we prepared a thick cathode with a sulfur loading of 4.9 mg cm^{-2} for high-loading measurements. As shown in Fig. 3c, the cell delivered a high initial areal capacity of 3.8 mA h cm^{-2} at a current density of 0.82 mA cm^{-2}. Even after 190 cycles, the device maintained a high reversible areal capacity of 2.7 mA h cm^{-2}, which surpasses the threshold value (2 mA h cm^{-2}) of a plug-in hybrid electrical vehicle. A comparison of the cycle performance observed in this work with data for Li–S batteries from recent studies based on high sulfur loadings is presented in Table S2.† We note that although the areal capacity of 3.8 mA h cm^{-2} reported here (Fig. 3c) is not the highest compared with some recently reported carbon-based electrodes with sophisticated cathode architectures, our slurry-derived electrodes exhibit a very high areal capacity with a prolonged cycling stability at a high sulfur loading. Moreover, the respectable electrochemical performance of CNT-S/TS-1 encouraged us to explore its practical applications. As shown in Fig. 3d, five half-cells were assembled in series and the battery pack could drive 90 indicators of an LED module, indicating the potential of the CNT-S/TS-1 electrode in a real-world application.

To further understand the superior electrochemical performance with respect to the discharge capacity, rate capability, and cycle stability, we investigated the interactions between TS-1 and LiPS by X-ray photoelectron spectroscopy (XPS) analysis of TS-1/LiPS (mainly Li_2S_6 as the representative soluble LiPS species) composites. In the high-resolution Li 1s spectrum of pristine Li_2S_6, a single component of Li–S was observed at 56.4 eV (Fig. 4a).[4,30] Upon contact with TS-1, this feature shifted to a lower binding energy of 56.2 eV, which indicated a strong chemical interaction, resulting from electron transfer from the TS-1 surface to the Li^+ ions. Concomitantly, the Ti 2p, O 1s, and Si 2p components shifted to higher binding energies for Li_2S_6 adsorbed on TS-1 (Fig. 4b, c and Fig. S9†), reconfirming strong chemical interactions between Li and TS-1.[31] As demonstrated previously, both the electrical conductivity and the LiPS/Li_2S affinity of the host materials affect the reaction kinetics of LiPS.[32] Herein, we posit that the Li bond formation for TS-1 facilitated intermolecular binding and charge transfer, which accounted for the enhanced redox kinetics. This mechanism is consistent with the observed electrochemical properties of the Li–S cell (Fig. 2 and 3). With respect to the high-resolution S 2p spectrum (Fig. 4d), pristine Li_2S_6 exhibited two main constituents corresponding to the terminal (S_T) and bridging (S_B) sulfur, respectively.[23,33,34] Interestingly, the S 2p spectroscopy negatively shifted by more than 0.3 eV, with the S_T moieties affected more than those of S_B, suggesting that the terminal S moieties captured more electronegative substances owing to electrostatic dipole–dipole interactions. Interestingly, we confirmed the existence of thiosulfite (165.5 eV) during the reaction.[35] On the basis of work by Nazar and co-workers, the presence of thiosulfite indicates a further reaction leading to the formation of insoluble Li_2S_2/Li_2S, and suggests that TS-1 has a

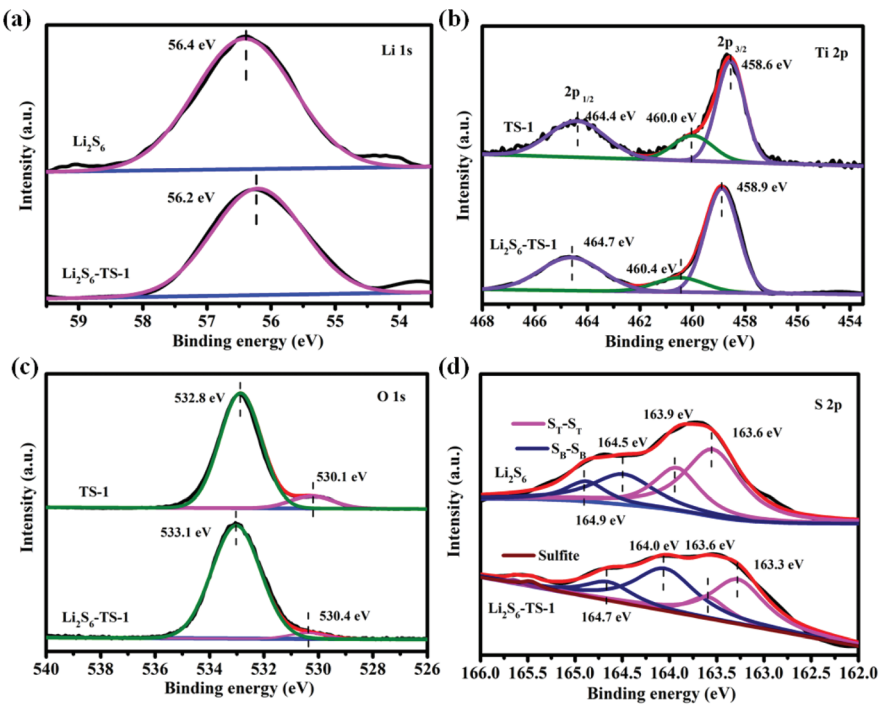

Fig. 4 Interfacial interactions between Li_2S_6 and TS-1. (a) Li 1s spectra of Li_2S_6 and Li_2S_6-TS-1. (b) Ti 2p and (c) O 1s spectra of TS-1 and Li_2S_6-TS-1. (d) S 2p spectra of Li_2S_6 and Li_2S_6-TS-1.

role in the LiPS transformation.[36] We note that the strong interfacial host–guest interactions might have two main effects on the sulfur electrochemistry: (1) promoting the immobilization of LiPS on the cathode and (2) favoring charge transfer from the substrates (CNTs/TS-1) to LiPS and their subsequent redox reactions. Herein, we assembled symmetric dummy cells composed of Li_2S_6 electrolyte between two identical electrodes. As shown in Fig. 5a, the current density in the CV curve increased by almost an order of magnitude after incorporation of TS-1. Nevertheless, the charge transfer (R_{ct}) of the CNT/TS-1 electrode was comparable to that of the CNT electrode owing to the intrinsic semi-conductive features of TS-1(Fig. 5b). Owing to the advantageous lithium-free features of the symmetric cells, we attribute this observation to the interfacial affinity and liquid–liquid conversion between TS-1 and LiPS. As clear evidence for this adsorption-induced promoted redox reaction, we used an H-type electrolytic cell to simulate the CV tests, as shown in Fig. 5c–f (see details in Experiment section). After 500 cycles, the color of the electrolytes of the CNT electrode slightly changed, indicating sluggish kinetics of the conversion between the various sulfur species on carbon substrates. The CNT/TS-1 electrode caused the color of the electrolyte solution to fade, indicating the catalytic conversion ability of TS-1 for LiPS. This promoted interfacial conversion induced by nonconductive substrate may probably be related to the balanced surface adsorption and diffusion of LiPS on the surface of TS-1, as recently demonstrated by Tao and co-workers.[7]

To further investigate the detailed speciation process of the sulfur-related species during cycling, we performed *in situ* UV-visible absorption spectroscopy based on a home-made cell to collect the information on the discharge products in real time, as schematically illustrated in Fig. S11.† The main reaction intermediates included S_8^{2-}, S_6^{2-}, S_4^{2-} and visible S_3^{*-} rad-

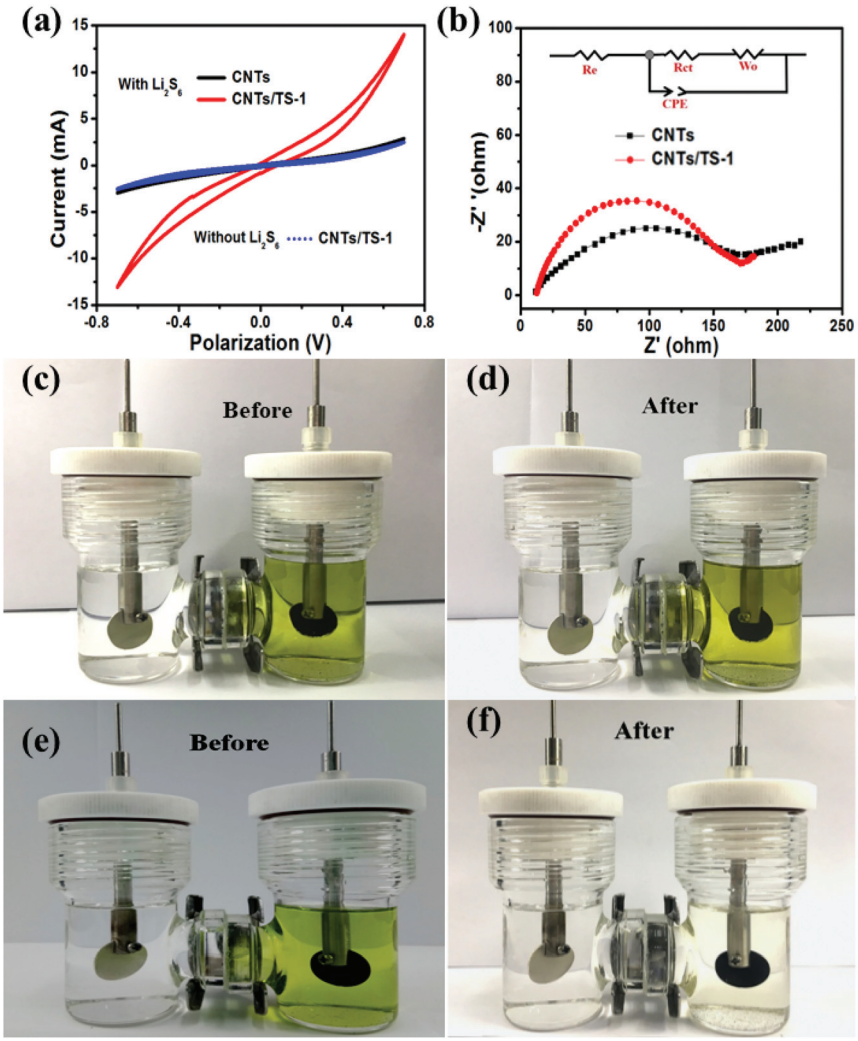

Fig. 5 (a) CV and (b) EIS of Li_2S_6–Li_2S_6 symmetrical cells. The inset of (b) is the fitting circuit of EIS spectra for symmetrical cells. The R_e represents electrolyte resistance, R_{ct} represents charge transfer, CPE and W represent the electrical double-layer capacitors on the surface of electrode and Warburg impedance, respectively. Digital photograph of the H-type mimic electrolytic cell for CV tests. (c, d) CNTs electrode before and after 500 CV cycles. (e, f) CNTs/TS-1 electrode before and after 500 CV cycles.

icals for both the CNT and CNT/TS-1 electrodes during the discharge process (Fig. 6a and b).[37–41] Hence, the co-existence of electrochemical and chemical reactions in the Li–S system, is consistent with recent mechanistic studies of sulfur chemistry.[42,43] On further inspection, a conspicuous lower content of S_8^{2-} species was observed for the CNT/TS-1 electrodes compared with the results for the CNT and bare glassy carbon electrodes (GCE). This result indicated rapid adsorption and conversion of soluble LiPS species at the CNT/TS-1 electrodes. As the process proceeded, two concave peaks at discharge voltages of 2.3 and 1.9 V were detected for S_8^{2-} species (Fig. 6c). Similar changes were also observed in S_6^{2-}, S_4^{2-}, and S_3^{2-} systems for the CNT/TS-1 electrodes. However, the concentrations of S_8^{2-}, S_6^{2-}, S_4^{2-}, and S_3^{2-} for the CNT electrode varied only slightly (Fig. 6c–f and Fig. S12†). Notably, the evolution sequence of S_3^{*-} radicals increased in intensity at a discharge depth of 2.3 V followed by a sharp increase at 1.9 V (Fig. 6f). The unique evolution of this behavior is very different from the cases of S_6^{2-}, S_4^{2-}, and S_3^{2-} in CNT/TS-1 electrodes. However, the CNT electrode showed a continuous consumption of S_3^{*-} radicals, as confirmed by the monotonic decrease in absorbance upon discharge. These observations indicated a faster dynamic equilibrium between S_8^{2-}, S_6^{2-}, and S_4^{2-} species and S_3^{*-} radicals in the CNT/TS-1 cathode compared with that in the CNT electrodes. The combined XPS, H-type, symmetric dummy cell analysis, and collective *in situ* UV-vis results, suggest that in the presence of TS-1, the S_3^{*-} radicals generated in the whole discharge process resulted from direct chemical transformations of S_8^{2-}, S_6^{2-}, and S_4^{2-}. Hence, the kinetics of transformations among sulfur species were substantially accelerated. To further confirm this mechanism, we conducted *in situ* UV-visible absorption spectra based on a nominal S_4^{2-} solution (Fig. S13†). Unlike the S_8^{2-} system, the S_4^{2-} showed continuous consumption throughout the dis-

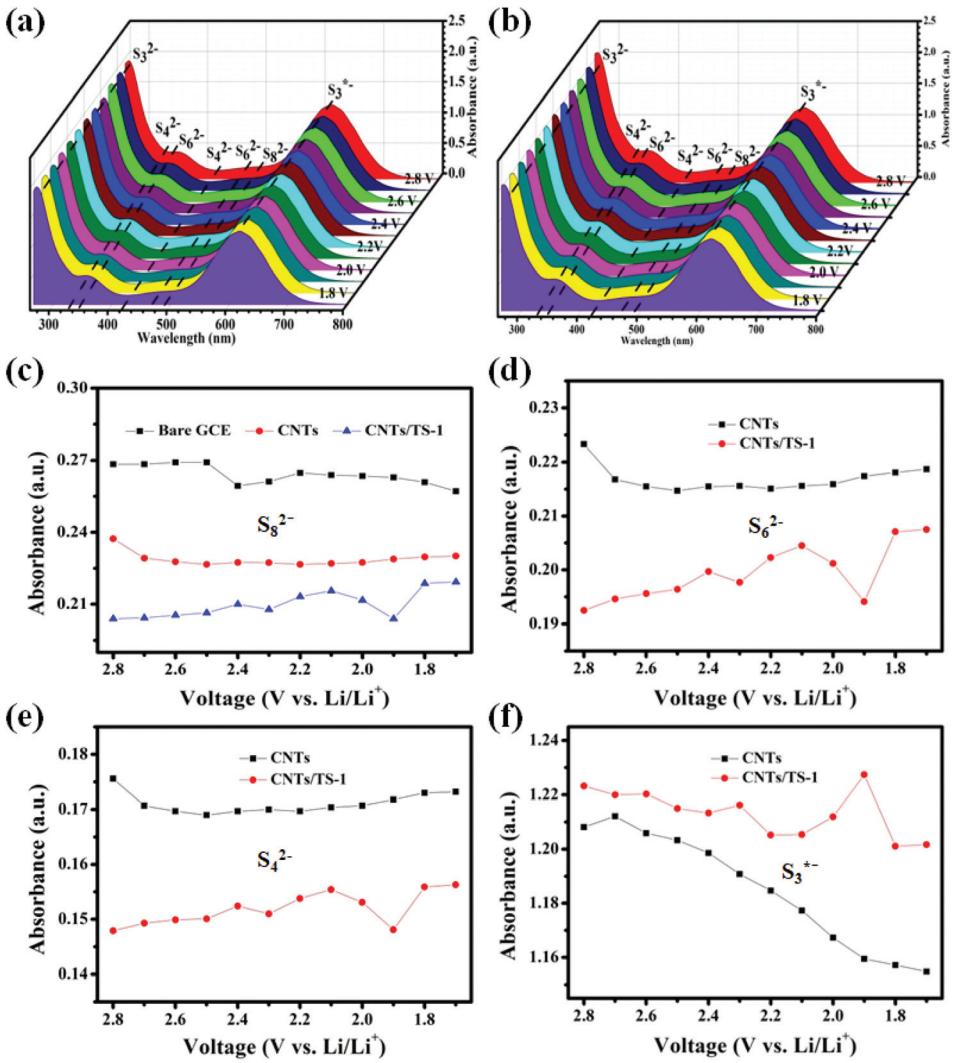

Fig. 6 The *in situ* UV/vis spectra of species during discharge process. (a) CNTs and (b) CNTs/TS-1 cell at various voltages in nominal S_8^{2-} solution (UV band attribution: S_8^{2-} at 492 nm, S_6^{2-} at 475 and 350 nm, S_4^{2-} at 420 and 325 nm, S_3^{2-} at 270 nm, S_3^{*-} at 617 nm). (c)–(f) Evolution of the UV-vis absorbance at 492, 475, 420 and 617 nm at various stages of the CV scanning in nominal S_8^{2-} solution.

charge process for the CNT/TS-1 electrode. However, a clear trend of S_3^{*-} radicals accumulation existed upon discharge. These observations were consistent with the S_3^{*-} radical-promoted reaction kinetics observed in the S_8^{2-} system, and further confirmed the fast and dynamic equilibrium between S_8^{2-} and S_3^{*-} radicals (Fig. 1).

On the basis of the abovementioned electrochemical data and *in situ* UV-vis results, we summarize the promoted redox reaction pathways of sulfur chemistry with the incorporation of TS-1, as schematically illustrated in Fig. 7. In the initial stage of discharge (at 2.8 V), long-chain S_8^{2-} species are first generated, which prompted adsorption of S_8^{2-} to occur at the reactive triple-phase interface among the TS-1, conductive CNT support, and electrolyte owing to the strong "polar–polar" interactions between TS-1 and LiPS (2.8–2.5 V). The trapped S_8^{2-}species quickly undergo disproportionation reactions to produce S_3^{*-} radicals and S_6^{2-}/S_4^{2-} anions (2.5–2.3 V). This mechanism explains the high concentration of S_3^{*-} radical observed in the initial discharge state, as shown in Fig. 6f. Notably, S_3^{*-} radicals are generally generated from the dissociation of S_6^{2-} anions ($S_6^{2-} = 2S_3^{*-}$);[36] however, in this case, the S_8^{2-}species trapped on the TS-1 surface directly convert into S_3^{*-} radicals possibly *via* the following disproportionation reaction: $2S_8^{2-} + 2e = 2S_3^{*-} + S_6^{2-} + S_4^{2-}$. The high nucleophilicity of the S_3^{*-} radicals promoted associative nucleophilic substitution reactions on the adsorbed S_6^{2-}/S_4^{2-} surface.[30] This result is supported by "Wackenroder reaction" theory where electroneutral elemental sulfur is also susceptible to nucleophilic attack by some electronegative groups in aqueous solution. The prompt conversion between S_8^{2-} and S_3^{*-} radicals is highly favorable for the subsequent evolution of S_6^{2-}/S_4^{2-} anions, where S_8^{2-}, S_6^{2-}, S_4^{2-} species, and S_3^{*-} radicals should temporarily reach an equilibrium ($S_8^{2-} + 2e = 2S_4^{2-}$; S_6^{2-} ($2S_3^{*-}$) = $3/2S_4^{2-}$), as supported by the inconspicuous variation of S_3^{*-}radicals from 2.5–2.3 V (Fig. 6f). As the discharge proceeded, the lithiation of S_6^{2-} and S_4^{2-} species induced consumption of S_3^{*-} radicals, leading to a continuous decrease of S_3^{*-} radicals at 2.2 V. The promoted liquid–liquid transformation (2.8–2.2 V) enriched S_4^{2-} species around the polar TS-1 surface, further affecting the correlated liquid–solid transformation at the end of the discharge (2.2–1.9 V), *i.e.*, the nucleation and growth processes of solid sulfides. Owing to the stable dynamic equilibrium between soluble sulfur species and S_3^{*-} radicals, further discharge to a lower voltage of 1.7 V led to complete electrochemical reduction of S_4^{2-} to solid Li_2S_2 and then to Li_2S, accompanied by a further decrease of the S_3^{*-} concentration. Overall, the faster dynamic equilibrium between S_8^{2-}, S_6^{2-}, S_4^{2-}, and S_3^{*-} radicals can be attrib-

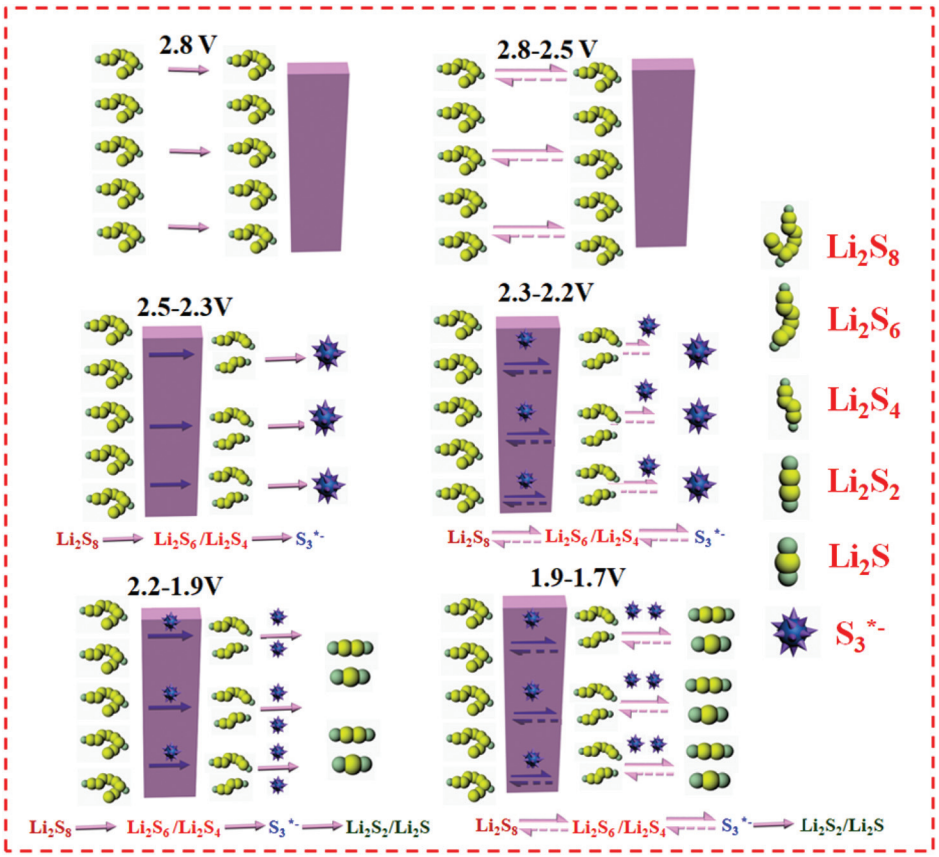

Fig. 7 Schematic illustration of the radicals-mediated LiPS conversion process in CNTs-S/TS-1 cathode and the possible reaction pathways based on the *in situ* UV-vis results.

uted to the chemical and electrochemical reactions at the CNT/TS-1 electrodes. In addition, the high catalytic formation of S_3^{*-} strengthened the comproportionation between S_8 and S^{2-}, leading to improved S_8 utilization.[44] These factors considerably enhanced the LiPS redox by facilitating preceding solid–liquid and consequent liquid–solid processes, mitigating polarization of the sulfur redox chemistry.

Conclusions

Commercially available TS-1 is applied as anchoring material for LiPS in Li–S batteries for the first time. We achieved remarkable performance, including a high specific capacity of 1459 mA h g^{-1} at 0.1C and a high areal capacity with a high sulfur loading of 4.9 mg cm^{-2}. Moreover, we used *in situ* UV-vis spectroscopy to clarify that the TS-1 promotes a radical-mediated redox process, where a direct transformation of S_8^{2-} species into S_3^{*-} radical occurs. Additionally, the rapid and dynamic equilibrium between S_8^{2-} species and S_3^{*-} radical promotes the redox reaction of LiPS intermediates and efficient regulation of nucleation and growth of solid sulfide precipitates. This simple yet effective modification of sulfur cathodes sheds light on the redox chemistry of sulfur species and realizes an accessible but efficient approach to improving the overall performance of Li–S batteries. This work promotes the pace of Li–S commercialization by offering a simple and cost-efficient method for improving electrochemical performance.

Conflicts of interest

There are no conflicts to declare.

Acknowledgements

The work was supported in part by grants from National Natural Science Foundation of China (51972238, 21875166, 51741207, 51572197), Natural Science Foundation of Zhejiang Province for Distinguished Young Scholars (LR18E020001), Science and Technology Project of Zhejiang Province (LGF18B050005), and Xinmiao talent project of Zhejiang Province (2019R429045).

Notes and references

1 H. Jiang, X. C. Liu, Y. Wu, Y. Shu, X. Gong, F. S. Ke and H. Deng, *Angew. Chem., Int. Ed.*, 2018, **57**, 3916–3921.
2 P. G. Bruce, S. A. Freunberger, L. J. Hardwick and J. M. Tarascon, *Nat. Mater.*, 2011, **11**, 19–29.
3 Y. X. Yin, S. Xin, Y. G. Guo and L. J. Wan, *Angew. Chem., Int. Ed.*, 2013, **52**, 13186–13200.
4 X. Ni, T. Qian, X. Liu, N. Xu, J. Liu and C. Yan, *Adv. Funct. Mater.*, 2018, **28**, 1706513.
5 Q. Pang, D. Kundu, M. Cuisinier and L. F. Nazar, *Nat. Commun.*, 2014, **5**, 4759.
6 Q. Pang, X. Liang, C. Y. Kwok and L. F. Nazar, *Nat. Energy*, 2016, **1**, 16132.
7 X. Tao, J. Wang, C. Liu, H. Wang, H. Yao, G. Zheng, W. S. Zhi, Q. Cai, W. Li and G. Zhou, *Nat. Commun.*, 2016, **7**, 11203.
8 D. Liu, C. Zhang, G. Zhou, W. Lv, G. Ling, L. Zhi and Q. H. Yang, *Adv. Sci.*, 2018, **5**, 1700270.
9 C. Ruan, Z. Yang, H. Nie, X. Zhou, Z. Guo, L. Wang, X. Ding, X. Chen and S. Huang, *Nanoscale*, 2018, **10**, 10999–11005.
10 W. Hua, Z. Yang, H. Nie, Z. Li, J. Yang, Z. Guo, C. Ruan, X. Chen and S. Huang, *ACS Nano*, 2017, **11**, 2209–2218.
11 Z. Xiao, Z. Yang, L. Zhou, L. Zhang and R. Wang, *ACS Appl. Mater. Interfaces*, 2017, **9**, 18845–18855.
12 Z. Sun, J. Zhang, L. Yin, G. Hu, R. Fang, H. M. Cheng and F. Li, *Nat. Commun.*, 2017, **8**, 14627.
13 X. Zhang, Z. Luo, P. Yu, Y. Cai, Y. Du, D. Wu, S. Gao, C. Tan, Z. Li, M. Ren, T. Osipowicz, S. Chen, Z. Jiang, J. Li, Y. Huang, J. Yang, Y. Chen, C. Y. Ang, Y. Zhao, P. Wang, L. Song, X. Wu, Z. Liu, A. Borgna and H. Zhang, *Nat. Catal.*, 2018, **1**, 460–468.
14 Y. Lai, H. Nie, X. Xu, G. Fang, X. Ding, D. Chan, S. Zhou, Y. Zhang, X. a. Chen and Z. Yang, *Acs Appl. Mater. Interfaces*, 2019, **11**, 29978–29984.
15 Z. Zhang, D.-H. Wu, Z. Zhou, G.-R. Li, S. Liu and X.-P. Gao, *Sci. China Mater.*, 2018, **62**, 74–86.
16 Y. T. Liu, D. D. Han, L. Wang, G. R. Li, S. Liu and X. P. Gao, *Adv. Energy Mater.*, 2019, **9**, 1803477.
17 J. Xiao, *Adv. Energy Mater.*, 2015, **5**, 1501102.
18 F. Pei, L. Lin, D. Ou, Z. Zheng, S. Mo, X. Fang and N. Zheng, *Nat. Commun.*, 2017, **8**, 482.
19 R. Fang, S. Zhao, P. Hou, M. Cheng, S. Wang, H. M. Cheng, C. Liu and F. Li, *Adv. Mater.*, 2016, **28**, 3374–3382.
20 Z. Song, X. Feng, N. Sheng, D. Lin, Y. Li, Y. Liu, X. Chen, X. Zhou, D. Chen and C. Yang, *Catal. Today*, 2018, DOI: 10.1016/j.cattod.2018.04.068.
21 M. Lin, C. Xia, B. Zhu, H. Li and X. Shu, *Chem. Eng. J.*, 2016, **295**, 370–375.
22 G. Lv, S. Deng, Y. Zhai, Y. Zhu, H. Li, F. Wang and X. Zhang, *Appl. Catal., A*, 2018, **567**, 28–35.
23 Z. Xiao, Z. Yang, Z. Li, P. Li and R. Wang, *ACS Nano*, 2019, **13**, 3404–3412.
24 X.-F. Yu, D.-X. Tian, W.-C. Li, B. He, Y. Zhang, Z.-Y. Chen and A.-H. Lu, *Nano Res.*, 2019, **12**, 1193–1197.
25 Z. Xiao, Z. Yang, L. Zhang, H. Pan and R. Wang, *ACS Nano*, 2017, **11**, 8488–8498.
26 Z. Guo, H. Nie, Z. Yang, W. Hua, C. Ruan, D. Chan, M. Ge, X. Chen and S. Huang, *Adv. Sci.*, 2018, **5**, 1800026.
27 Z. Xiao, Z. Yang, L. Wang, H. Nie, M. Zhong, Q. Lai, X. Xu, L. Zhang and S. Huang, *Adv. Mater.*, 2015, **27**, 2891–2898.
28 J. Zhou, T. Qian, N. Xu, M. Wang, X. Ni, X. Liu, X. Shen and C. Yan, *Adv. Mater.*, 2017, **29**, 1701294.
29 Z. Deng, Z. Zhang, Y. Lai, J. Liu, J. Li and Y. Liu, *J. Electrochem. Soc.*, 2013, **160**, A553–A558.

30 Q. Pang, D. Kundu and L. F. Nazar, *Mater. Horiz.*, 2016, **3**, 130–136.
31 Y. Mi, W. Liu, K. R. Yang, J. Jiang, Q. Fan, Z. Weng, Y. Zhong, Z. Wu, G. W. Brudvig, V. S. Batista, H. Zhou and H. Wang, *Angew. Chem., Int. Ed.*, 2016, **55**, 14818–14822.
32 H. J. Peng, G. Zhang, X. Chen, Z. W. Zhang, W. T. Xu, J. Q. Huang and Q. Zhang, *Angew. Chem., Int. Ed.*, 2016, **55**, 12990–12995.
33 X. Liang, Y. Rangom, C. Y. Kwok, Q. Pang and L. F. Nazar, *Adv. Mater.*, 2017, **29**, 1603040.
34 Z. Y. Wang, L. Wang, S. Liu, G. R. Li and X. P. Gao, *Adv. Funct. Mater.*, 2019, **29**, 1901051.
35 B. J. Lindberg, K. Hamrin, G. Johansson, U. Gelius, A. Fahlman, C. Nordling and K. Siegbahn, *Phys. Scr.*, 1970, **1**, 286.
36 X. Liang, C. Hart, Q. Pang, A. Garsuch, T. Weiss and L. F. Nazar, *Nat. Commun.*, 2015, **6**, 5682.
37 Q. Zou and Y. C. Lu, *J. Phys. Chem. Lett.*, 2016, **7**, 1518–1525.
38 N. S. Manan, L. Aldous, Y. Alias, P. Murray, L. J. Yellowlees, M. C. Lagunas and C. Hardacre, *J. Phys. Chem. B*, 2011, **115**, 13873–13879.
39 D. S. Shin, N. Doddapaneni and M. P. Su, *Inorg. Chem.*, 1992, **31**, 4060–4064.
40 K. Ayako, S. Soichi, Y. Yoshinari, A. Ryuichi and T. Toshikazu, *Phys. Chem. Chem. Phys.*, 2014, **16**, 9344–9350.
41 R. D. Rauh, F. S. Shuker, J. M. Marston and S. B. Brummer, *J. Inorg. Nucl. Chem.*, 1977, **39**, 1761–1766.
42 Q. Wang, J. Zheng, E. Walter, H. Pan, D. Lv, P. Zuo, H. Chen, Z. D. Deng, B. Y. Liaw, X. Yu, X. Yang, J.-G. Zhang, J. Liu and J. Xiao, *J. Electrochem. Soc.*, 2015, **162**, A474–A478.
43 C. Barchasz, F. Molton, C. Duboc, J. C. Lepretre, S. Patoux and F. Alloin, *Anal. Chem.*, 2012, **84**, 3973–3980.
44 G. Li, S. Wang, Y. Zhang, M. Li, Z. Chen and J. Lu, *Adv. Mater.*, 2018, **30**, 1705590.